

A saturation-absorption rubidium magnetometer with multilevel optical Bloch-equation modeling for intermediate-to-high fields

Mayand Dangi,^{1,*} Prateek Rajan Gupta,² Joseph Kasti,¹ Nivedan Vishwanath,³ Michael Zepp,³ David Smith,³ Benedikt Geiger,³ and Jennifer T. Choy^{1,2,†}

¹*Department of Electrical and Computer Engineering,*

University of Wisconsin-Madison, Madison, Wisconsin 53706, USA

²*Department of Physics, University of Wisconsin-Madison, Madison, Wisconsin 53706, USA*

³*Department of Nuclear Engineering and Engineering Physics,*

University of Wisconsin-Madison, Madison, Wisconsin 53706, USA

(Dated: January 15, 2026)

We present SASHMAG (Saturated Absorption Spectroscopy High-field MAGnetometer), an atomic sensor designed for precision magnetic-field measurements in the intermediate-to-high field regime (> 0.2 T) using Rubidium-87 (^{87}Rb). The sensor operates in the hyperfine Paschen-Back regime, where the hyperfine and Zeeman interactions decouple, and utilizes counter-propagating pump-probe configuration in Faraday geometry to resolve isolated, Doppler-free Zeeman transitions. To interpret the resulting spectra in this strongly field-dependent regime, we developed a comprehensive multilevel optical Bloch-equation model solved explicitly in the uncoupled $|m_I, m_J\rangle$ basis, capturing state mixing and nonlinear saturation dynamics. This model reproduces measured spectra at sub-Doppler resolution and is consistent with analytical expectations for power broadening and thermal Doppler scaling. Magnetic field estimation is performed using a physics-constrained optimization routine that infers the magnetic field by minimizing the residual between experimentally extracted line centers and calculated transition frequencies from the field-dependent Hamiltonian. We demonstrate magnetic field retrieval from 0.2 T to 0.4 T with a precision of ± 0.0017 T. Furthermore, the validated simulation establishes a foundation for generating synthetic training datasets, paving the way for autonomous, Machine Learning-enhanced magnetometry in applications ranging from MRI to fusion reactors.

I. INTRODUCTION

Intermediate-to-high magnetic fields, spanning the sub-tesla regime to tens of tesla, play a central role across a wide range of applications including ultra-high-field magnetic resonance imaging (MRI) [1–3], condensed-matter and quantum materials studies [4–7], and large-scale magnet systems for particle colliders [8–10] and fusion [11–13]. Across these settings, accurate magnetic-field diagnostics are challenging because sensors must operate reliably under temperature variations, electromagnetic interference, radiation, and strong field gradients. Atomic sensors are attractive in this context because they enable field-dependent optical readout referenced to inherently stable atomic structure and, when paired with physics-based forward models, can mitigate biases from environmental perturbations. In this work, we present SASHMAG (Saturated Absorption Spectroscopy High-field MAGnetometer), designed for precision magnetic-field measurements in the intermediate-to-high field regime (> 0.2 T) using ^{87}Rb vapor.

While a number of mature magnetic-field sensors exist, each carries limitations in this operating space. Hall-effect probes have been the workhorse for magnetic-field sensing due to their wide dynamic range, compactness, and vector capability. In practice, however, their abso-

lute accuracy is limited by calibration uncertainty, thermal drift, radiation damage, and susceptibility to electromagnetic interference [14]. Fluxmeter inductive coils offer excellent sensitivity to changes in magnetic flux, but do not directly provide an absolute magnetic field without an external reference and are ultimately limited by integration drift [15].

Magneto-optical Faraday rotation magnetometers provide an electrically passive alternative, but quantitative measurements depend on material-specific Verdet constants with strong wavelength and temperature dependence, requiring careful calibration and environmental control [16].

Vapor-cell alkali magnetometry offers an attractive route to absolute field measurement because field-dependent line splitting can be traced to atomic constants and optical frequency references. High-field atomic spectroscopy was pioneered in extreme pulsed-power environments [17, 18] and extended to the 10–100 T regime through sodium-emission-line spectroscopy on pulsed high-current platforms [19, 20]. Compact alkali-vapor sensors have been demonstrated in 58 T pulsed fields using microsized samples [21, 22]. At intermediate field fields, nanocell and thin cells provide high spatial resolution, but Doppler-free features depend on the nanoscale cell geometry [23, 24]. Extending atomic magnetometry toward MRI-relevant field strengths, Stærkind et al. demonstrated a high-field optical cesium magnetometer within a 7-T MRI scanner by tracking a single extreme-state resonance [25, 26]. In contrast, our approach tar-

* mdangi2@wisc.edu

† jennifer.choy@wisc.edu

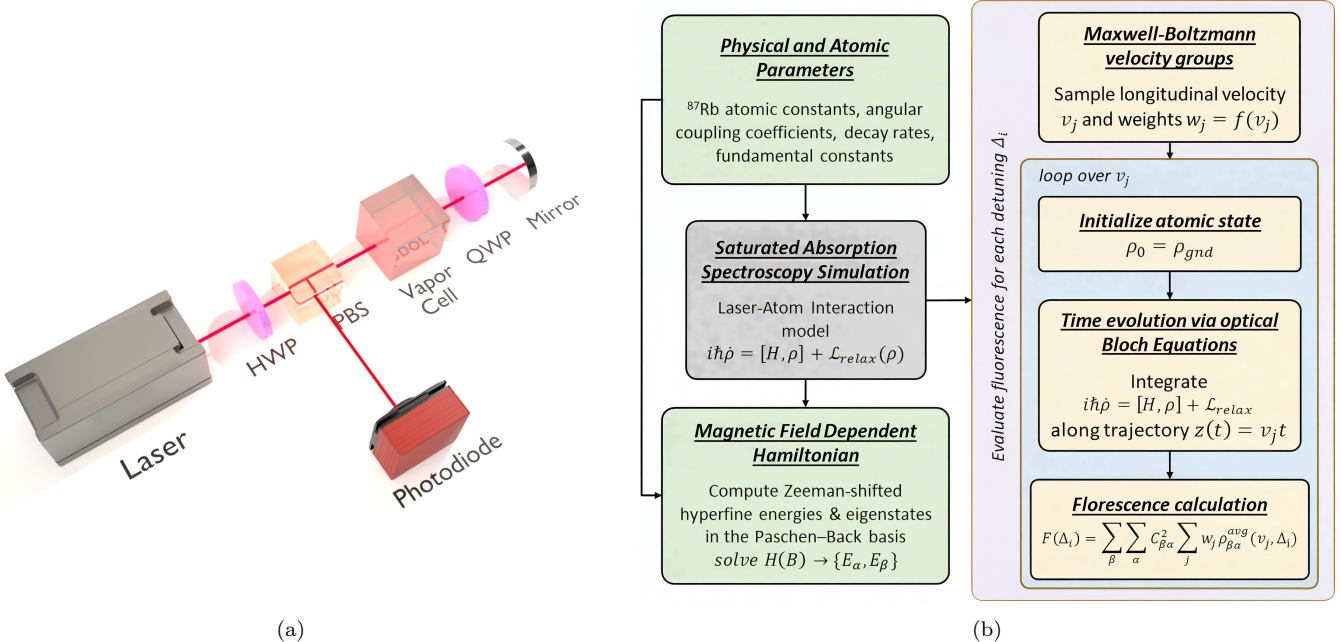


FIG. 1. (a) Experimental setup for saturated absorption spectroscopy (SAS) of the ^{87}Rb . (b) Computational workflow for modeling high-field SAS using an optical Bloch equation framework.

gets the intermediate-to-high-field regime in rubidium using pump-probe saturated absorption spectroscopy in a conventional vapor cell, enabling field inference from a spectrum of sub-Doppler Zeeman transitions without requiring thin-cell methods or single-line tracking.

While sub-Doppler spectroscopy resolves individual transitions and enhances sensitivity to magnetic-field-induced shifts [27, 28], quantitative magnetometry in the intermediate to high field regime requires models that include multilevel saturation and field-induced mixing. Existing tools such as ElecSus [29, 30] accurately fit Doppler-broadened linear spectra for absolute field extraction [31, 32], but do not capture the nonlinear multilevel dynamics required to quantitatively interpret Doppler-free spectra in crowded, strongly mixed high-field regimes. Here we address that need with a multilevel OBE model solved in the uncoupled $|m_I, m_J\rangle$ basis, enabling high-fidelity forward simulation and physics-constrained field extraction. In experiments we demonstrate magnetic-field inference up to 0.4T with 0.42 mT/ $\sqrt{\text{Hz}}$ sensitivity, while the model framework remains applicable to substantially higher fields. Furthermore, the OBE model presented here can be used to generate high-fidelity synthetic datasets, providing a foundation for training machine learning algorithms for future autonomous sensing systems.

II. THEORETICAL MODELING

A. Hyperfine Paschen-Back Hamiltonian and Basis Selection

Our modeling here spans the transition from Zeeman regime into the hyperfine Paschen-Back regime (HPB). For ^{87}Rb in intermediate-to-high-field, the Zeeman interaction becomes comparable to (or can exceed) hyperfine coupling, so total angular momentum F is no longer conserved and the eigenstates must be described in an uncoupled basis ($|m_I, m_J\rangle$). We numerically diagonalize the full Hamiltonian (H):

$$H = H_0 + H_{\text{hfs}} + H_B \quad (1)$$

where H_0 is the unperturbed atomic Hamiltonian, H_{hfs} is the hyperfine interaction term, and H_B is the Zeeman interaction term describing the coupling to the external magnetic field B . The numerical solution yields the precise eigenvalues of the states and the eigenstates as the linear combination of uncoupled basis states $|m_I, m_J\rangle$.

B. Saturated Absorption Spectroscopy Modeling

To model the saturated absorption spectroscopy in the presence of a strong magnetic field, we extend the density matrix framework of Maguire et al., which was originally developed for ^{85}Rb in a zero field in the $|F, m_F\rangle$ basis [28] and is adapted here for the hyperfine Paschen-Back regime of ^{87}Rb in the $|m_I, m_J\rangle$ basis. Our framework

enables the simulation of ^{87}Rb SAS spectra in large magnetic fields in the $|m_I, m_J\rangle$ basis. We consider the D_2 transition ($5^2S_{1/2} \rightarrow 5^2P_{3/2}$), which involves a total of $N = 24$ magnetic sublevels. The indices $\alpha = \{1, 2, \dots, 8\}$ label the ground-state sublevels of the $5^2S_{1/2}$ manifold, while $\beta = \{9, 10, \dots, 24\}$ label the excited-state sublevels of the $5^2P_{3/2}$ manifold. It incorporates the magnetic field-dependent atomic Hamiltonian, polarization-selective (e.g., $\sigma\pm$) transitions, and Doppler averaging based on a Maxwell-Boltzmann velocity distribution.

Following Maguire et al. (with full derivation provided in Appendix A), the density-matrix evolution in the rotating frame can be written as [28]:

$$\dot{\rho}_{\alpha\alpha} = 2 \cos(kz) \sum_{\beta=9}^{24} \Omega_{\beta\alpha} \text{Im}(\tilde{\rho}_{\beta\alpha}) + \frac{1}{\tau} \sum_{\beta=9}^{24} (C_{\beta\alpha})^2 \rho_{\beta\beta} \quad (2)$$

$$\dot{\rho}_{\beta\beta} = -2 \cos(kz) \sum_{\alpha=1}^8 \Omega_{\beta\alpha} \text{Im}(\tilde{\rho}_{\beta\alpha}) - \frac{1}{\tau} \rho_{\beta\beta} \quad (3)$$

$$\begin{aligned} \dot{\tilde{\rho}}_{\beta\alpha} = & i\Omega_{\beta\alpha} \cos(kz)(\rho_{\beta\beta} - \rho_{\alpha\alpha}) - i(\omega_{\beta\alpha} - \omega)\tilde{\rho}_{\beta\alpha} - \\ & \frac{1}{2\tau} \tilde{\rho}_{\beta\alpha} \quad (\text{for } \alpha \neq \beta) \end{aligned} \quad (4)$$

Here, $\rho_{\alpha\alpha}$ and $\rho_{\beta\beta}$ represent the populations of the ground and excited states, respectively, while $\tilde{\rho}_{\beta\alpha}$ denotes the slowly varying optical coherence in the rotating frame. The quantity $\omega_{\beta\alpha}$ is the magnetic-field-dependent atomic transition frequency, ω is the laser angular frequency, k is the optical wave vector, and τ is the excited-state lifetime. The $C_{\beta\alpha}$ represents angular coupling coefficients for the transition from β to α and the rabi frequency ($\Omega_{\beta\alpha}$) is defined as [28]:

$$\Omega_{\beta\alpha} = C_{\beta\alpha} \left(\frac{3\pi\epsilon_0}{k^3\tau\hbar} \right)^{\frac{1}{2}} E \quad (5)$$

where E is the electric field amplitude of the traveling wave, ϵ_0 is vacuum permittivity and \hbar is reduced Planck constant.

The full description of the atomic system involves an $N \times N$ matrix of coupled equations (Eqs. (2) - (4)), where $N = 24$. This results in a total of 576 equations, which is computationally demanding to solve directly. However, the system can be significantly simplified by considering selection rules and inherent symmetries of the problem. First, the hermiticity of the density matrix, $\rho_{\beta\alpha} = \rho_{\alpha\beta}^*$, reduces the problem to $N(N+1)/2$. Second, the model is significantly simplified by the fact that the optical field, $H_{\beta\alpha}^I$, does not drive coherences between levels within the same manifold. Consequently, all ground-ground and excited-excited coherences vanish, meaning only the diagonal population elements within these manifolds need to be retained. And the light-atom interaction term $H_{\beta\alpha}^I$ is non-zero only for ground-excited pairs directly connected

by the dipole selection rules ($\Delta m_J = \pm 1$) determined by the laser polarization. Applying these physical and mathematical constraints reduces the original 576 equations to a manageable set of 40 coupled differential equations.

C. Numerical Solution and Calculation of SAS Signal

We applied the Runge-Kutta method to solve the system of coupled differential equations. The density matrix $\rho(v, \Delta, t)$ gives the number of atoms in each of their internal states at time t for a certain velocity v and laser detuning Δ . Fig. I illustrates the computational workflow used to obtain the numerical solution.

The observed SAS spectrum represents an effective absorption signal that is derived from the total fluorescence emitted by an ensemble of atoms. This fluorescence is averaged over time and the Maxwellian velocity distribution, and the fluorescence resulting from the decay of a single excited state, denoted as β , is expressed in [28]:

$$F_\beta = \sum_{\alpha} C_{\beta\alpha}^2 \rho_{\beta\beta} \quad (6)$$

The total fluorescence signal $F(\Delta)$, which represents the ensemble-averaged absorption measured at a given laser detuning Δ , is calculated by summing the contributions from all excited states β ($\sum_{\beta} F_{\beta}$) after performing the velocity-averaging step:

$$F(\Delta) = \sum_{\beta} \sum_{\alpha} C_{\beta\alpha}^2 \sum_i f(v_i) \rho_{\beta\beta}^{\text{avg}}(v_i, \Delta) \quad (7)$$

Here, $f(v_i)$ is the Maxwellian probability for velocity group v_i , and $\rho_{\beta\beta}^{\text{avg}}(v_i, \Delta)$ is the time-averaged excited-state population calculated from the OBE for that velocity group. The detuning Δ is defined as the frequency difference between the laser frequency ω_L and the centered frequency ω_0 of the $5^2S_{1/2} \rightarrow 5^2P_{3/2}$ fine structure transition, $\Delta = \omega_L - \omega_0$.

III. EXPERIMENTAL SETUP

The experimental setup, illustrated in Fig. 2, is based on a standard Saturated Absorption Spectroscopy (SAS) configuration utilizing two counter-propagating pump and probe beams. The optical setup comprises two distinct sections: Reference Optics for frequency calibration and a Main Experiment Arm for high magnetic field measurements.

The light source is a Photodigm Distributed Bragg Reflector (DBR) Laser, tuned to the D_2 transition line of ^{87}Rb ($\lambda \approx 780.241$ nm). An Optical Isolator (OI) prevents back-reflections from reaching the laser cavity. The output beam is initially split into two paths. A half-wave

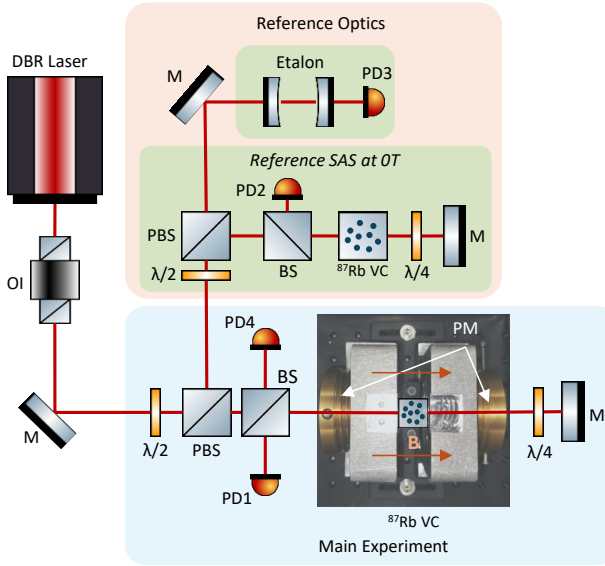


FIG. 2. Optical schematic of the experimental setup for saturated absorption spectroscopy (SAS) of ^{87}Rb . The light from the DBR Laser is split into two arms. The Reference Optics arm (top, orange section) provides coarse frequency markers using an Etalon and a stable, low-field (0 T) SAS lock signal using a separate ^{87}Rb cell and **PD2** for frequency positioning. The Main Experiment arm (bottom, blue section) performs the high magnetic field SAS measurement. This arm features the primary ^{87}Rb vapor cell (**VC**) placed in a Faraday geometry between two permanent magnets (**PM**) configured in a quasi-Helmholtz arrangement. The field-dependent spectrum is detected at **PD1**. Key components include: **OI** (Optical Isolator), **M** (Mirror), $\lambda/2$ (Half Waveplate) and $\lambda/4$ (Quarter Waveplate), **PBS** (Polarizing Beam Splitter), **BS** (Beam Splitter), and **PD** (Photodiode).

plate and a Polarizing Beam Splitter (PBS) are used to direct the light into the Reference Arm and the Main Experiment Arm. The light source provides a mode-hop-free spectral scan range of approximately 30 GHz. This wide range is crucial, as it enables the simultaneous capture of multiple widely separated atomic transitions characteristic of the Hyperfine Paschen-Back regime.

The Reference Arm serves two essential functions for frequency calibration. First, a portion of the reference beam is directed through a Thorlabs Fabry-Perot Interferometer to produce frequency markers for coarse frequency axis calibration. Second, another portion of the reference beam is directed into a conventional Reference SAS setup containing a separate ^{87}Rb cell at zero field. This zero-field spectrum is used for calibrating the zero detuning position of the high-field SAS spectrum.

The Main Experiment Arm measures the ^{87}Rb spectrum under a strong magnetic field. The sensor head consists of isotopically pure ^{87}Rb contained within a 12 mm \times 12 mm \times 12 mm vapor cell.

An external longitudinal magnetic field ranging from 0.2 T to 0.4 T is generated using two permanent N42

ring magnets. Each magnet has 2 inches of outer diameter, 0.25 inches of inner diameter, and a thickness of 1 inch, and they are configured in a quasi-Helmholtz arrangement. Each magnet has an outer diameter of 2 inches, an inner diameter of 0.25 inches, and a thickness of 1 inch, and they are configured in a quasi-Helmholtz arrangement. The basic magnetic housing design was adapted from the magnetic field configuration scheme described in Ref. [33], and the CAD model was redesigned to accommodate the chosen magnet dimensions. This specific configuration was engineered to withstand the substantial attractive forces between the two permanent magnets as well as achieve a uniform field distribution across the vapor cell.

The vapor cell is in a Faraday geometry, where the direction of light propagation is parallel to the applied magnetic field, resulting in the selection rule of $\Delta m_j = \pm 1$. To stabilize the atomic vapor density and enhance the overall signal-to-noise ratio (SNR), the cell is actively heated and maintained at a temperature of 40°C.

IV. RESULTS AND ANALYSIS

A. Frequency Calibration and Experimental Spectra

Experimental validation was performed using the experimental setup described in Sec III. The calibration of the DAQ system's time axis to the frequency detuning scale is established using the reference optical assembly illustrated in 2. The Etalon serves as a precise frequency ruler, and the reference SAS pack at 0T provides the absolute frequency reference.

To construct the frequency axis, the etalon signal from

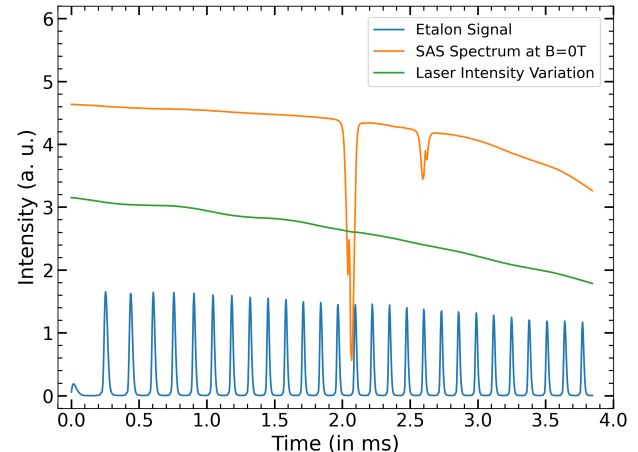


FIG. 3. Frequency calibration and reference signals. The blue trace shows the Fabry-Perot transmission peaks (detected by PD3). The orange trace (top) is the saturated absorption spectrum (SAS) of the ^{87}Rb D_2 line at zero field (PD2). The green trace (PD4) monitors the change in laser intensity during the ramping of the laser.

PD3 undergoes preprocessing with a Savitzky-Golay filter, which preserves the etalon peaks while eliminating high-frequency noise. Subsequently, a peak detection algorithm from SciPy is employed to identify the coarse peaks. To surpass the resolution limit imposed by the DAQ system sampling rate, the precise center of each etalon peak was determined via a sub-pixel parabolic fit to the local maxima. This procedure yields a set of time indices corresponding to frequency markers separated by exactly 1.5 GHz. The full continuous frequency axis, $\nu(t)$, was generated by linearly interpolating between the identified peaks, thereby correcting for any non-linearities in the laser-scanning mechanism. Finally the absolute detuning $\Delta = 0$ tied to the unperturbed $^{87}\text{Rb } 5S_{1/2} \rightarrow 5P_{3/2}$ transition energy, determined from the reference SAS at 0T (Fig. 3).

With the frequency axis calibrated, we characterized the SASHMAG sensor response by mechanically adjusting the permanent magnet separation to tune the transverse magnetic field (0.2 T – 0.4 T). The device operates in the Faraday geometry, where the quantization axis is parallel to the applied magnetic field (B), and the linearly polarized probe beam decomposes into σ^+ and σ^- components. The resulting experimental signals (Fig. 4(b)) confirm the sensing principle: as the magnetic field increases, the σ^+ and σ^- manifolds diverge symmetrically, creating a widely separated, Doppler-free spectral fingerprint.

B. Theoretical Modeling and Experimental Validation

The spectral response of the ^{87}Rb system was first modeled using the Optical Bloch Equation (OBE) formalism to establish a theoretical baseline. The atomic properties, including transition strengths, natural lifetimes, and hyperfine splitting constants, were obtained from the standard reference for $^{87}\text{Rb } D$ line data [34]. The simulation parameters were constrained to match the experimental conditions: a probe beam waist (w_0) of 0.84 mm, an incident pump power of 6 mW, and a temperature of 313K (40°C).

Figure 4(a) presents the simulated saturated absorption spectrum calculated at a magnetic field of $B = 0.4092$ T. This precise field value was determined via the spectral optimization algorithm (detailed in Sec. IV C) and is consistent with independent measurements taken with a Hall probe sensor (≈ 0.4 T). The model successfully predicts the resonance positions and the relative absorption depths. The specific transitions associated with each resolved peak are tabulated in Tables I and II, labeled in the uncoupled Paschen-Back basis $|m_I, m_J\rangle$.

Beyond peak positions, the OBE model captures the fundamental broadening mechanisms inherent to the system:

- **Power Broadening:** The atom-light interaction strength is governed by the Rabi frequency,

TABLE I. σ^- transitions corresponding to the labeled peaks in Fig. 4(a), with detunings of the $^{87}\text{Rb } D_2$ line for $B = 0.4092$ T.

Index	Detuning (MHz)	Transition	
		Initial State	Final State
1	-12186.73	$ +\frac{3}{2}, +\frac{1}{2}\rangle$	$ +\frac{3}{2}, -\frac{1}{2}\rangle$
2	-10995.19	$ +\frac{1}{2}, +\frac{1}{2}\rangle$	$ +\frac{1}{2}, -\frac{1}{2}\rangle$
3	-9616.43	$ -\frac{1}{2}, +\frac{1}{2}\rangle$	$ -\frac{1}{2}, -\frac{1}{2}\rangle$
4	-7898.86	$ -\frac{3}{2}, -\frac{1}{2}\rangle$	$ -\frac{3}{2}, -\frac{3}{2}\rangle$
5	-7905.06	$ -\frac{3}{2}, +\frac{1}{2}\rangle$	$ -\frac{3}{2}, -\frac{1}{2}\rangle$
6	-5553.14	$ -\frac{1}{2}, -\frac{1}{2}\rangle$	$ -\frac{1}{2}, -\frac{3}{2}\rangle$
7	-4001.62	$ +\frac{1}{2}, -\frac{1}{2}\rangle$	$ +\frac{1}{2}, -\frac{3}{2}\rangle$
8	-2786.95	$ +\frac{3}{2}, -\frac{1}{2}\rangle$	$ +\frac{3}{2}, -\frac{3}{2}\rangle$

TABLE II. σ^+ transitions corresponding to the labeled peaks in Fig. 4(a), with detunings of the $^{87}\text{Rb } D_2$ line for $B = 0.4092$ T.

Index	Detuning (MHz)	Transition	
		Initial State	Final State
1	3357.96	$ +\frac{3}{2}, -\frac{1}{2}\rangle$	$ +\frac{3}{2}, +\frac{1}{2}\rangle$
2	4369.00	$ +\frac{1}{2}, -\frac{1}{2}\rangle$	$ +\frac{1}{2}, +\frac{1}{2}\rangle$
3	5577.04	$ -\frac{1}{2}, -\frac{1}{2}\rangle$	$ -\frac{1}{2}, +\frac{1}{2}\rangle$
4	6927.47	$ -\frac{3}{2}, +\frac{1}{2}\rangle$	$ -\frac{3}{2}, +\frac{3}{2}\rangle$
5	7134.37	$ -\frac{3}{2}, -\frac{1}{2}\rangle$	$ -\frac{3}{2}, +\frac{1}{2}\rangle$
6	9654.02	$ -\frac{1}{2}, +\frac{1}{2}\rangle$	$ -\frac{1}{2}, +\frac{3}{2}\rangle$
7	11373.56	$ +\frac{1}{2}, +\frac{1}{2}\rangle$	$ +\frac{1}{2}, +\frac{3}{2}\rangle$
8	12742.01	$ +\frac{3}{2}, +\frac{1}{2}\rangle$	$ +\frac{3}{2}, +\frac{3}{2}\rangle$

$\Omega \propto \mathbf{d} \cdot \mathbf{E}$, leading to intensity-dependent spectral broadening. To characterize this effect and validate the model's saturation parameters, we analyzed the lineshape of the $|1/2, -1/2\rangle \rightarrow |1/2, -3/2\rangle$ transition at two distinct pump intensities: $I_{low} = 4.96 \text{ kW/m}^2$ and $I_{high} = 27.1 \text{ kW/m}^2$ (see Fig. 5(a)). Lorentzian fits were applied to the simulated data profiles to extract the Full Width at Half Maximum (FWHM). The ratio of the measured intensity broadening, $\Delta\omega_{FWHM}(I_{high})/\Delta\omega_{FWHM}(I_{low})$, was determined to be 0.423. This value agrees extremely well with the theoretical ratio of 0.428 obtained from the standard power-broadening expression derived for a driven two-level system, $\Delta\omega_{FWHM} = \Gamma\sqrt{1 + I/I_{sat}}$ [35], confirming that the OBE model accurately captures the non-linear saturation dy-

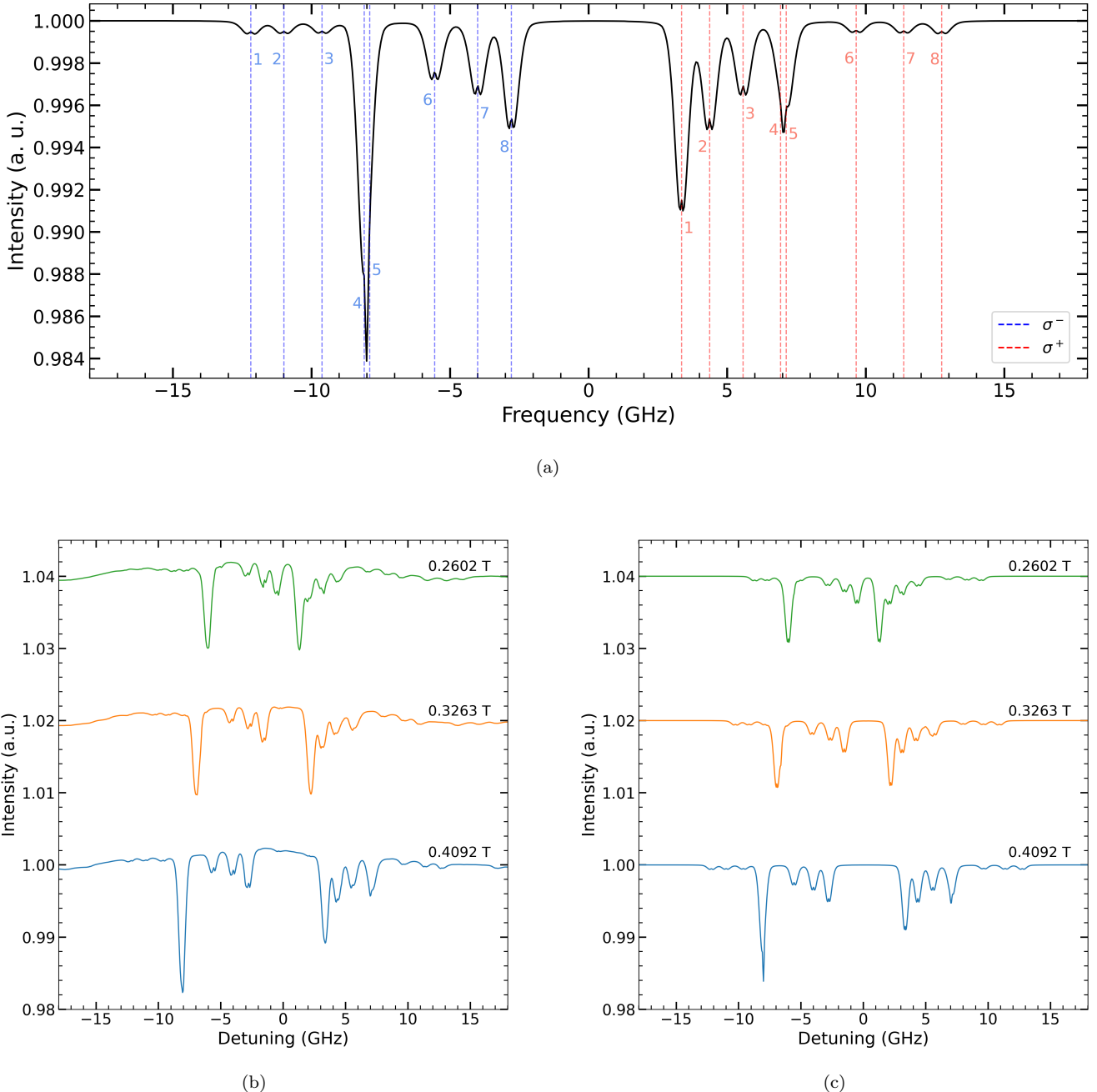


FIG. 4. (a) Stimulated saturated absorption spectra at magnetic field $B = 0.4092$ T (b) Experimental spectra obtained for the ^{87}Rb D_2 transition at magnetic fields of 0.2602 T, 0.3263 T, and 0.4092 T (from top to bottom). (c) Corresponding simulated spectra calculated using the Optical Bloch Equation (OBE) model at the same field strengths. All traces are vertically offset for clarity.

namics of the system.

- **Doppler Broadening:** The model takes into account of longitudinal Maxwell-Boltzmann velocity distribution $f(v, T)$. To validate this thermal averaging, we simulated the spectral envelope at $T = 300$ K and $T = 600$ K of the $|3/2, -1/2\rangle \rightarrow |3/2, -3/2\rangle$ transition (see Fig. 5(b)). The ex-

tracted Full Width at Half Maximum (FWHM) values were found to be 559 ± 19 MHz and 771 ± 40 MHz, respectively. The ratio of these widths is 0.726, which stands in excellent agreement with the theoretical scaling ratio of $\sqrt{300/600} \approx 0.707$ expected for a Doppler-dominated profile. This confirms that the simulation accurately captures the characteristic \sqrt{T} dependence of the inhomoge-

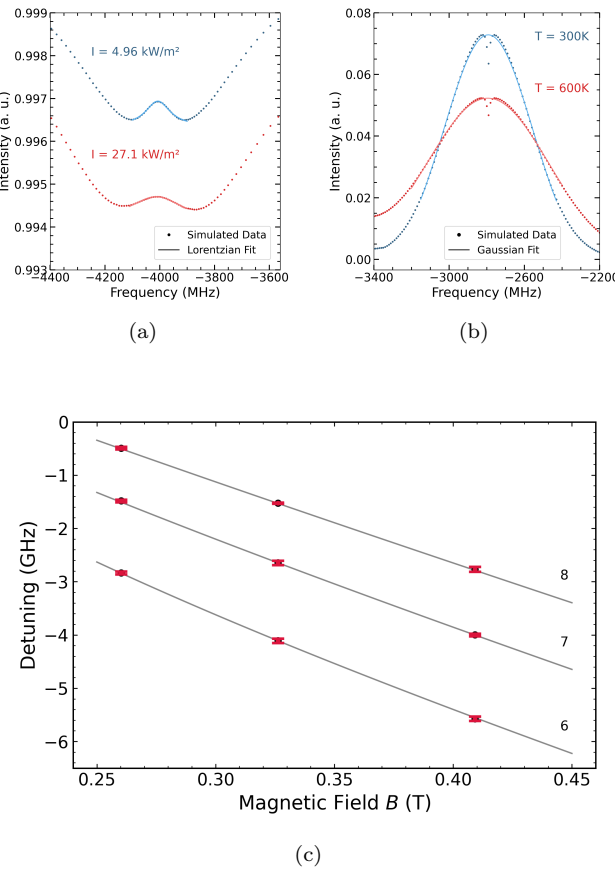


FIG. 5. (a) Simulated spectra showing power broadening at $I = 4.96 \text{ kW/m}^2$ and 27.1 kW/m^2 . (b) Doppler-broadened profiles at $T = 300 \text{ K}$ (blue) and 600 K (red). (c) Calculated σ -transition detunings are shown as a function of the applied magnetic field B (gray solid lines). Red circles indicate experimentally extracted resonance positions at $B = 0.2602 \text{ T}$, 0.3263 T , and 0.4092 T , with vertical error bars representing the combined 1σ uncertainty from frequency calibration and peak fitting. Transitions 6, 7, and 8 belong to the $|m_J = -1/2\rangle \rightarrow |m'_J = -3/2\rangle$ manifold with $m_I = -1/2, +1/2$, and $+3/2$, respectively..

geneous broadening.

The simulation effectively predicts the shape of the spectrum, as well as the effects of Doppler and power broadening. However, the model does not consider collisional broadening, since its contribution is small compared to Doppler and power broadening at the pressures maintained in the vapor cell. The model considers changes in the velocity distribution with temperature; however, it does not account for the increase in atomic number density that is governed by the vapor pressure of rubidium. As a result, absolute signal amplitudes are treated as normalized parameters.

C. Magnetic Field Estimation and Sensitivity

The quantitative estimation of the magnetic field is performed via a physics-constrained spectral optimization algorithm [36]. The saturated absorption peaks from the experimental SAS spectra $\nu_{\text{exp}}^{(k)}$ are extracted from fitting Gaussian profiles to each SAS peak. These experimental positions are compared against the theoretical transition frequencies, $\nu_{\text{theo}}(B)$, derived from the diagonalization of the Hamiltonian H described in eq. 1. We define a scalar loss function $L(B)$ based on the least-squares residual:

$$L(B) = \sum_k \left(\nu_{\text{exp}}^{(k)} - \nu_{\text{theo}}^{(k)}(B) \right)^2 \quad (8)$$

A bounded minimization routine optimizes the field parameter B to minimize $L(B)$, effectively converting the spectral data to a local magnetic field.

To rigorously quantify the measurement confidence, the uncertainties in the estimated fields were evaluated using a Monte Carlo (MC) error-propagation approach. We model each experimental peak position $\nu_{\text{exp}}^{(k)}$ as an independent random variable following a Gaussian distribution with standard deviation σ_k . The total uncertainty for each peak is calculated by combining the statistical fitting error ($\sigma_{\text{fit}}^{(k)}$) and the global frequency axis calibration uncertainty (σ_{calib}) in quadrature:

$$\sigma_k = \sqrt{(\sigma_{\text{fit}}^{(k)})^2 + (\sigma_{\text{calib}})^2} \quad (9)$$

For each MC trial j , we generate N_{MC} synthetic datasets by randomly perturbing the experimental peak positions according to:

$$\nu_{\text{exp,MC}}^{(k,j)} = \nu_{\text{exp}}^{(k)} + \delta_{k,j}, \quad \delta_{k,j} \sim \mathcal{N}(0, \sigma_k) \quad (10)$$

For each MC trial j , the optimization routine minimizes $L(B)$ to yield a trial field estimate B_j . The final reported magnetic field uncertainty is defined as the standard deviation of the resulting distribution of estimated fields $\{B_j\}_{j=1}^{N_{\text{MC}}}$.

Using this technique, the magnetic field was estimated for the three experimental configurations shown in Fig. 4(b). The analysis yielded field values of $0.4092 \pm 0.0017 \text{ T}$, $0.3263 \pm 0.0016 \text{ T}$, and $0.2602 \pm 0.0016 \text{ T}$ and sensitivity of $0.42 \text{ mT}/\sqrt{\text{Hz}}$. The consistent precision across the dynamic range demonstrates the robustness of the SASHMAG.

V. CONCLUSION

In this paper, we demonstrate SASHMAG for measuring magnetic fields in the high-magnetic-field Paschen-Back (HPB) regime. By using a counter-propagating pump-probe setup in the Faraday geometry, we successfully resolved the Zeeman transitions where the nuclear

and electronic spins are decoupled. This provides a clear, linear spectral signal suitable for high-field metrology.

The magnetic field estimation was performed using a physics-based optimization method (Sec. IV C). This routine minimizes the difference between experimental peak positions and theoretical values calculated from the Hamiltonian in the uncoupled $|m_I, m_J\rangle$ basis. Our approach yielded consistently precise field extraction across the dynamic range from 0.2 to 0.4 T (limited by the strength of our DC magnets) with an uncertainty of $\pm 0.41\%$. Achieving this precision by directly solving the inverse problem is a vital capability for high-field applications.

We also validated a Multilevel Optical Bloch Equation (OBE) model in the HPB regime, which is essential to accurately capture the detailed spectrum and the significant saturation effects that occur in a high-power, high-field environment. We confirmed the model's accuracy by comparing it against fundamental non-linear physics: the observed power broadening ratio (0.423) and the Doppler broadening thermal scaling (0.726) matched our analytical predictions precisely.

VI. FUTURE OUTLOOK

The future development of SASHMAG will focus on enhancing the sensor's performance and achieving full system autonomy. We aim to develop optical interrogation schemes that increase both measurement sensitivity and bandwidth. Bandwidth improvement is particularly critical for capturing transient magnetic field fluctuations in dynamic environments. We plan to deploy a Machine Learning (ML) method to create a completely autonomous sensing system. Since the OBE model validated in this work accurately captures the signal behavior, it will be used to generate massive, high-quality synthetic datasets for training purposes. We will train neural networks on this data to automatically detect peak positions and estimate the magnetic field without human intervention. This hybrid approach, combining rigorous atomic physics with the speed of AI, will enable robust, real-time magnetometry suitable for advanced industrial and scientific applications.

ACKNOWLEDGMENTS

This work was supported by the US Department of Energy (DE-SC0024471). This work utilized computational resources provided by the Center for High Throughput Computing (CHTC) at the University of Wisconsin–Madison. The authors acknowledge the use of CHTC services supported by the University of Wisconsin–Madison[37]. We also acknowledge the University of Wisconsin–Madison Design and Innovation Lab for assistance with the fabrication of experimental

components.

Appendix A: Derivation of Optical Bloch Equations

The time evolution of the density matrix elements, derived from the Liouville-von Neumann equation, is given by:

$$\dot{\rho}_{\beta\alpha} = -i\omega_{\beta\alpha}\rho_{\beta\alpha} - \frac{i}{\hbar} \sum_{\gamma} (H_{\beta\gamma}^I \rho_{\gamma\alpha} - \rho_{\beta\gamma} H_{\gamma\alpha}^I) \quad (A1)$$

Phenomenological decay terms are added to account for spontaneous emission and decoherence:

$$-\frac{1}{2\tau} \rho_{\beta\alpha} \quad \text{for } \dot{\rho}_{\beta\alpha} (\beta \neq \alpha) \quad (A2)$$

$$-\frac{1}{\tau} \rho_{\beta\beta} \quad \text{for } \dot{\rho}_{\beta\beta} \quad (A3)$$

$$+\frac{1}{\tau} \sum_{\beta} (C_{\beta\alpha})^2 \rho_{\beta\beta} \quad \text{for } \dot{\rho}_{\alpha\alpha} \quad (A4)$$

Here, the ground states are defined by $\alpha \in \{1, \dots, 8\}$ and the excited states by $\beta \in \{9, \dots, 24\}$.

Following the transformation of the off-diagonal elements to a rotating frame defined by the atom-laser coupling frequency ω , we define the tilde matrix elements:

$$\tilde{\rho}_{\beta\alpha} = \begin{cases} \rho_{\beta\alpha} e^{i\omega t} & (\beta \neq \alpha), \\ \rho_{\beta\alpha} & (\beta = \alpha). \end{cases} \quad (A5)$$

1. Ground-State Diagonals ($\dot{\rho}_{\alpha\alpha}$)

For the time evolution of the ground-state diagonals, $\dot{\rho}_{\alpha\alpha}$, using equation (A1) and including the phenomenological decay and repopulation terms:

$$\dot{\rho}_{\alpha\alpha} = -\frac{i}{\hbar} \sum_{\gamma} (H_{\alpha\gamma}^I \rho_{\gamma\alpha} - \rho_{\alpha\gamma} H_{\gamma\alpha}^I) + \frac{1}{\tau} \sum_{\beta} (C_{\beta\alpha})^2 \rho_{\beta\beta} \quad (A6)$$

Since the interaction Hamiltonian H^I couples only between ground states (α) and excited states (β), the summation over γ reduces to only the excited states β :

$$\dot{\rho}_{\alpha\alpha} = -\frac{i}{\hbar} \sum_{\beta} (H_{\alpha\beta}^I \rho_{\beta\alpha} - \rho_{\alpha\beta} H_{\beta\alpha}^I) + \frac{1}{\tau} \sum_{\beta} (C_{\beta\alpha})^2 \rho_{\beta\beta} \quad (A7)$$

The interaction Hamiltonian matrix element is defined as:

$$H_{\beta\alpha}^I = \hbar\Omega_{\beta\alpha}\hat{E} \quad (A8)$$

where $\hat{E} = \cos(kz)(e^{i\omega t} + e^{-i\omega t})$. Since $\rho_{\alpha\beta} = \rho_{\beta\alpha}^*$, the first term in Equation (A7) simplifies as follows:

$$\begin{aligned} -\frac{i}{\hbar} \sum_{\beta} (H_{\alpha\beta}^I \rho_{\beta\alpha} - \rho_{\alpha\beta} H_{\beta\alpha}^I) \\ = -\frac{i}{\hbar} \sum_{\beta} (H_{\alpha\beta}^I \rho_{\beta\alpha} - \rho_{\alpha\beta} H_{\beta\alpha}^I) \\ = -\frac{i}{\hbar} \sum_{\beta} (\hbar \Omega_{\alpha\beta} \hat{E} \rho_{\beta\alpha} - \rho_{\alpha\beta} \hbar \Omega_{\beta\alpha} \hat{E}) \\ = -i \sum_{\beta} \Omega_{\beta\alpha} (\hat{E} \rho_{\beta\alpha} - \rho_{\alpha\beta} \hat{E}) \end{aligned} \quad (\text{A9})$$

$$\begin{aligned} -\frac{i}{\hbar} \sum_{\beta} (H_{\alpha\beta}^I \rho_{\beta\alpha} - \rho_{\alpha\beta} H_{\beta\alpha}^I) \\ = -i \sum_{\beta} \Omega_{\beta\alpha} (\hat{E} \rho_{\beta\alpha} - \rho_{\alpha\beta} \hat{E}) \\ = -i \cos(kz) \sum_{\beta} \Omega_{\beta\alpha} (e^{i\omega t} + e^{-i\omega t}) (\rho_{\beta\alpha} - \rho_{\beta\alpha}^*) \end{aligned} \quad (\text{A10})$$

Next, we substitute $\rho_{\beta\alpha} = \tilde{\rho}_{\beta\alpha} e^{-i\omega t}$ and apply the Rotating Wave Approximation (RWA), which drops terms evolving at $e^{\pm 2i\omega t}$:

$$\begin{aligned} -\frac{i}{\hbar} \sum_{\beta} (H_{\alpha\beta}^I \rho_{\beta\alpha} - \rho_{\alpha\beta} H_{\beta\alpha}^I) \\ = -i \cos(kz) \sum_{\beta} \Omega_{\beta\alpha} (e^{i\omega t} + e^{-i\omega t}) (\rho_{\beta\alpha} - \rho_{\beta\alpha}^*) \\ = -i \cos(kz) \sum_{\beta} \Omega_{\beta\alpha} (e^{i\omega t} + e^{-i\omega t}) (\tilde{\rho}_{\beta\alpha} e^{-i\omega t} - \tilde{\rho}_{\beta\alpha}^* e^{i\omega t}) \\ = 2 \cos(kz) \sum_{\beta} \Omega_{\beta\alpha} \text{Im}(\tilde{\rho}_{\beta\alpha}) \end{aligned} \quad (\text{A11})$$

Substituting this simplified term back into Equation (A7) yields the final equation for the ground-state diagonals:

$$\dot{\rho}_{\alpha\alpha} = 2 \cos(kz) \sum_{\beta} \Omega_{\beta\alpha} \text{Im}(\tilde{\rho}_{\beta\alpha}) + \frac{1}{\tau} \sum_{\beta} (C_{\beta\alpha})^2 \rho_{\beta\beta} \quad (\text{A12})$$

2. Excited-State Diagonals ($\dot{\rho}_{\beta\beta}$)

For the time evolution of the excited-state diagonals, we start from the master equation,

$$\dot{\rho}_{\beta\beta} = -\frac{i}{\hbar} \sum_{\gamma} (H_{\beta\gamma}^I \rho_{\gamma\beta} - \rho_{\beta\gamma} H_{\gamma\beta}^I) - \frac{1}{\tau} \rho_{\beta\beta}, \quad (\text{A13})$$

and note that the interaction Hamiltonian couples only excited states β to ground states α . Thus, the sum reduces to

$$\dot{\rho}_{\beta\beta} = -\frac{i}{\hbar} \sum_{\alpha} (H_{\beta\alpha}^I \rho_{\alpha\beta} - \rho_{\beta\alpha} H_{\alpha\beta}^I) - \frac{1}{\tau} \rho_{\beta\beta}. \quad (\text{A14})$$

Using the definition of the interaction Hamiltonian, $H_{\beta\alpha}^I = \hbar \Omega_{\beta\alpha} \hat{E}$ with $\hat{E}(z, t) = \cos(kz)(e^{i\omega t} + e^{-i\omega t})$, the first term becomes

$$\begin{aligned} -\frac{i}{\hbar} \sum_{\alpha} (H_{\beta\alpha}^I \rho_{\alpha\beta} - \rho_{\beta\alpha} H_{\alpha\beta}^I) \\ = -i \cos(kz) \sum_{\alpha} \Omega_{\beta\alpha} (e^{i\omega t} + e^{-i\omega t}) (\rho_{\alpha\beta} - \rho_{\beta\alpha}). \end{aligned} \quad (\text{A15})$$

We now transform to the rotating frame using the definition of eq. A5

$$\rho_{\beta\alpha} = \tilde{\rho}_{\beta\alpha} e^{-i\omega t}, \quad \rho_{\alpha\beta} = \tilde{\rho}_{\beta\alpha}^* e^{i\omega t}.$$

Substituting these and applying the RWA gives,

$$(e^{i\omega t} + e^{-i\omega t})(\rho_{\alpha\beta} - \rho_{\beta\alpha}) = \tilde{\rho}_{\beta\alpha}^* - \tilde{\rho}_{\beta\alpha} = -2i \text{Im}(\tilde{\rho}_{\beta\alpha})$$

Thus, the coherent contribution becomes

$$\begin{aligned} -i \cos(kz) \sum_{\alpha} \Omega_{\beta\alpha} (\tilde{\rho}_{\beta\alpha}^* - \tilde{\rho}_{\beta\alpha}) \\ = -2 \cos(kz) \sum_{\alpha} \Omega_{\beta\alpha} \text{Im}(\tilde{\rho}_{\beta\alpha}). \end{aligned} \quad (\text{A16})$$

Substituting this into Eq. (A14), we obtain the final form for the excited-state diagonal elements:

$$\dot{\rho}_{\beta\beta} = -2 \cos(kz) \sum_{\alpha} \Omega_{\beta\alpha} \text{Im}(\tilde{\rho}_{\beta\alpha}) - \frac{1}{\tau} \rho_{\beta\beta} \quad (\text{A17})$$

3. Off-Diagonal Elements ($\dot{\rho}_{\beta\alpha}$, $\beta \neq \alpha$)

Equation A1 gives us the time evolution of the off-diagonal density-matrix elements, which includes terms for phenomenological coherence decay.

For general indices, if β is not equal to α ,

$$\dot{\rho}_{\beta\alpha} = -i\omega_{\beta\alpha} \rho_{\beta\alpha} - \frac{i}{\hbar} \sum_{\gamma} (H_{\beta\gamma}^I \rho_{\gamma\alpha} - \rho_{\beta\gamma} H_{\gamma\alpha}^I) - \frac{1}{2\tau} \rho_{\beta\alpha} \quad (\text{A18})$$

where $\omega_{\beta\alpha} = \omega_{\beta} - \omega_{\alpha}$. Considering the rotating frame transformation as described in Eq. A5 we have:

$$\tilde{\rho}_{\beta\alpha} = \rho_{\beta\alpha} e^{i\omega t} \quad (\text{A19})$$

differentiating both sides w.r.t time

$$\dot{\tilde{\rho}}_{\beta\alpha} = \dot{\rho}_{\beta\alpha} e^{i\omega t} + i\omega \rho_{\beta\alpha} e^{i\omega t} \quad (\text{A20})$$

Rearranging the terms will give us,

$$\dot{\rho}_{\beta\alpha} = (\dot{\tilde{\rho}}_{\beta\alpha} - i\omega \tilde{\rho}_{\beta\alpha}) e^{-i\omega t} \quad (\text{A21})$$

Substituting eq. A21 into eq. A18

$$\begin{aligned} (\dot{\tilde{\rho}}_{\beta\alpha} - i\omega \tilde{\rho}_{\beta\alpha}) e^{-i\omega t} &= -i\omega_{\beta\alpha} \rho_{\beta\alpha} \\ &- \frac{i}{\hbar} \sum_{\gamma} (H_{\beta\gamma}^I \rho_{\gamma\alpha} - \rho_{\beta\gamma} H_{\gamma\alpha}^I) - \frac{1}{2\tau} \rho_{\beta\alpha} \end{aligned} \quad (\text{A22})$$

$$\begin{aligned} \dot{\tilde{\rho}}_{\beta\alpha} - i\omega\tilde{\rho}_{\beta\alpha} &= -i\omega_{\beta\alpha}\underbrace{\tilde{\rho}_{\beta\alpha}e^{i\omega t}}_{\tilde{\rho}_{\beta\alpha}} - \frac{1}{2\tau}\underbrace{\tilde{\rho}_{\beta\alpha}e^{i\omega t}}_{\tilde{\rho}_{\beta\alpha}} \\ &\quad - \frac{i}{\hbar}\sum_{\gamma}\left(H_{\beta\gamma}^I\underbrace{\tilde{\rho}_{\gamma\alpha}e^{i\omega t}}_{\tilde{\rho}_{\gamma\alpha}} - \underbrace{\tilde{\rho}_{\beta\gamma}e^{i\omega t}}_{\tilde{\rho}_{\beta\gamma}}H_{\gamma\alpha}^I\right) \end{aligned} \quad (\text{A23})$$

$$\begin{aligned} \dot{\tilde{\rho}}_{\beta\alpha} &= -i(\omega_{\beta\alpha} - \omega)\tilde{\rho}_{\beta\gamma} - \frac{1}{2\tau}\tilde{\rho}_{\beta\gamma} \\ &\quad - \frac{i}{\hbar}\sum_{\gamma}\left(H_{\beta\gamma}^I\tilde{\rho}_{\gamma\alpha} - \tilde{\rho}_{\beta\gamma}H_{\gamma\alpha}^I\right) \end{aligned} \quad (\text{A24})$$

Given that the laser is in resonance with the $\alpha \leftrightarrow \beta$ transition. In the initial term of the summation, the dominant contribution occurs when $\gamma = \alpha$, yielding: $\sum_{\gamma} H_{\beta\gamma}^I \tilde{\rho}_{\beta\gamma} \approx H_{\beta\alpha}^I \tilde{\rho}_{\alpha\alpha}$. Similarly, for the subsequent term: The dominant contribution occurs when $\gamma = \beta$, giving $\sum_{\gamma} H_{\beta\gamma}^I \tilde{\rho}_{\beta\gamma} \approx H_{\beta\alpha}^I \tilde{\rho}_{\beta\beta}$. Thus,

$$\dot{\tilde{\rho}}_{\beta\alpha} = i\Omega_{\beta\alpha} \cos(kz)(\rho_{\beta\beta} - \rho_{\alpha\alpha}) - i(\omega_{\beta\alpha} - \omega)\tilde{\rho}_{\beta\alpha} - \frac{1}{2\tau}\tilde{\rho}_{\beta\alpha} \quad (\text{A25})$$

4. Angular Coupling Coefficients

The dipole matrix element $\langle g | H^I | e \rangle$ is given by[38]:

$$\begin{aligned} \langle g | H^I | e \rangle &= \langle nL \| er \| n'L' \rangle (-1)^{L'-1+m_L} \sqrt{2L+1} \\ &\quad \begin{pmatrix} L' & 1 & L \\ m_{L'} & q & -m_L \end{pmatrix} \times \delta_{s,s'} \delta_{m_s, m'_{s'}}. \end{aligned} \quad (\text{A26})$$

Here $\langle nL \| er \| n'L' \rangle$ is the *reduced dipole matrix element*, and the *angular coupling coefficient* for any photon polarization ($q = 0, \pm 1$) is given by:

$$C_q = (-1)^{L'-1+m_L} \sqrt{2L+1} \begin{pmatrix} L' & 1 & L \\ m_{L'} & q & -m_L \end{pmatrix} \quad (\text{A27})$$

[1] O. Kraff, A. Fischer, A. M. Nagel, C. Mönninghoff, and M. E. Ladd, Mri at 7 tesla and above: demonstrated and potential capabilities, *Journal of Magnetic Resonance Imaging* **41**, 13 (2015).

[2] S. Trattnig, E. Springer, W. Bogner, G. Hangel, B. Strasser, B. Dymerska, P. L. Cardoso, and S. D. Robinson, Key clinical benefits of neuroimaging at 7 t, *Neuroimage* **168**, 477 (2018).

[3] T. Okada, K. Fujimoto, Y. Fushimi, T. Akasaka, D. H. Thuy, A. Shima, N. Sawamoto, N. Oishi, Z. Zhang, T. Funaki, *et al.*, Neuroimaging at 7 tesla: a pictorial narrative review, *Quantitative imaging in medicine and surgery* **12**, 3406 (2022).

[4] V. Zapf, M. Jaime, and C. Batista, Bose-einstein condensation in quantum magnets, *Reviews of Modern Physics* **86**, 563 (2014).

[5] N. P. Ong and L. Li, Quantum matter in ultrahigh magnetic fields (2021), arXiv:2103.09155 [cond-mat].

[6] S. K. Lewin, C. E. Frank, S. Ran, J. Paglione, and N. P. Butch, A review of ute2 at high magnetic fields, *Reports on Progress in Physics* **86**, 114501 (2023).

[7] M. V. Kartsovnik, High magnetic fields: a tool for studying electronic properties of layered organic metals, *Chemical reviews* **104**, 5737 (2004).

[8] L. Bottura, S. Prestemon, L. Rossi, and A. V. Zlobin, Superconducting magnets and technologies for future colliders, *Frontiers in Physics* **10**, 935196 (2022).

[9] T. Shen, L. Garcia Fajardo, C. Myers, A. Hafalia Jr, J. L. Rudeiros Fernández, D. Arbelaez, L. Brouwer, S. Caspi, P. Ferracin, S. Gourlay, *et al.*, Design, fabrication, and characterization of a high-field high-temperature superconducting bi-2212 accelerator dipole magnet, *Physical Review Accelerators and Beams* **25**, 122401 (2022).

[10] M. g 2 Collaboration *et al.*, Magnetic-field measurement and analysis for the muon g-2 experiment at fermilab, *Physical Review A* **103**, 042208 (2021).

[11] G. Vayakis, S. Arshad, D. Delhom, A. Encheva, T. Giacomini, L. Jones, K. M. Patel, M. Pérez-Lasala, M. Portales, D. Prieto, F. Sartori, S. Simrock, J. A. Snipes, V. S. Uditsev, C. Watts, A. Winter, and L. Zabeo, Development of the ITER magnetic diagnostic set and specificationa), *Review of Scientific Instruments* **83**, 10D712 (2012).

[12] Y. Ma, G. Vayakis, L. B. Begrambekov, J. J. Cooper, I. Duran, M. Hirsch, H. P. Laqua, P. Moreau, J. W. Oosterbeek, P. Spuig, T. Stange, and M. Walsh, Design and development of ITER high-frequency magnetic sensor, *Fusion Engineering and Design* **112**, 594 (2016).

[13] P. Moreau, A. Le-Luyer, P. Spuig, P. Malard, F. Saint-Laurent, J. F. Artaud, J. Morales, B. Faugeras, H. Heumann, B. Cantone, M. Moreau, C. Brun, R. Nouilletas, E. Nardon, B. Santraine, A. Berne, P. Kuman, S. Belsare, and WEST Team, The new magnetic diagnostics in the WEST tokamak, *Review of Scientific Instruments* **89**, 10J109 (2018).

[14] I. Lake Shore Cryotronics, F71 and f41 teslameter specifications, <https://www.lakeshore.com/products/categories/specification/magnetic-products/gaussmeters-teslameters/f71-and-f41-teslameters>, accessed: 2025-12-26.

[15] M. Buzio, Fabrication and calibration of search coils, arXiv preprint arXiv:1104.0803 (2011).

[16] S. Tsuji-Lio, T. Akiyama, E. Sato, T. Nozawa, H. Tsutsui, R. Shimada, M. Takahashi, and K. Terai, Fiberoptic heterodyne magnetic field sensor for long-pulsed fusion devices, *Review of Scientific Instruments* **72**, 413 (2001).

[17] W. Garn, R. Caird, D. Thomson, and C. Fowler, Technique for measuring megagauss magnetic fields using zeeman effect, *Review of Scientific Instruments* **37**, 762 (1966).

[18] M. Gomez, S. Hansen, K. Peterson, D. Bliss, A. Carlson, D. Lamppa, D. Schroen, and G. Rochau, Magnetic field measurements via visible spectroscopy on the z machine, *Review of Scientific Instruments* **85**, 11E609 (2014).

[19] J. Banasek, J. Engelbrecht, S. Pikuz, T. Shelkovenko, and D. Hammer, Measuring 10–20 t magnetic fields in single wire explosions using zeeman splitting, *Review of Scientific Instruments* **87**, 103506 (2016).

[20] J. Banasek, J. Engelbrecht, S. Pikuz, T. Shelkovenko, and D. Hammer, Measuring 20–100 t b-fields using zeeman splitting of sodium emission lines on a 500 ka pulsed power machine, *Review of Scientific Instruments* **87**, 11D407 (2016).

[21] S. George, N. Bruyant, J. Béard, S. Scotto, E. Arimondo, R. Battesti, D. Ciampini, and C. Rizzo, Pulsed high magnetic field measurement with a rubidium vapor sensor, *Review of Scientific Instruments* **88**, 073102 (2017).

[22] D. Ciampini, R. Battesti, C. Rizzo, and E. Arimondo, Optical spectroscopy of a micro-sized rb vapor sample in magnetic fields up to 58 t, *Physical Review A* **96**, 052504 (2017).

[23] E. Klinger, H. Azizbekyan, A. Sargsyan, C. Leroy, D. Sarkisyan, and A. Papoyan, Proof of the feasibility of a nanocell-based wide-range optical magnetometer, *Applied Optics* **59**, 2231 (2020).

[24] A. Sargsyan, G. Hakhumyan, A. Tonoyan, P. Petrov, and T. Vartanyan, Study of the rb d 2-line splitting in a strong transverse magnetic field with doppler-free spectroscopy in a nanocell, *Optics and Spectroscopy* **119**, 202 (2015).

[25] H. Stærkind, K. Jensen, J. H. Müller, V. O. Boer, E. T. Petersen, and E. S. Polzik, Precision measurement of the excited state landé g-factor and diamagnetic shift of the cesium d 2 line, *Physical Review X* **13**, 021036 (2023).

[26] H. Stærkind, K. Jensen, J. H. Müller, V. O. Boer, E. S. Polzik, and E. T. Petersen, High-field optical cesium magnetometer for magnetic resonance imaging, *PRX Quantum* **5**, 020320 (2024).

[27] S. Scotto, D. Ciampini, C. Rizzo, and E. Arimondo, Four-level n-scheme crossover resonances in rb satu-
ration spectroscopy in magnetic fields, arXiv preprint arXiv:1509.06978 (2015).

[28] L. P. Maguire, R. M. Bijnen, E. Mese, and R. E. Scholten, Theoretical calculation of saturated absorption spectra for multi-level atoms, *Journal of Physics B: Atomic, Molecular and Optical Physics* **39**, 2709–2720 (2006).

[29] M. A. Zentile, J. Keaveney, L. Weller, D. J. Whiting, C. S. Adams, and I. G. Hughes, Elecsus: A program to calculate the electric susceptibility of an atomic ensemble, *Computer Physics Communications* **189**, 162 (2015).

[30] J. Keaveney, C. S. Adams, and I. G. Hughes, Elecsus: Extension to arbitrary geometry magneto-optics, *Computer physics communications* **224**, 311 (2018).

[31] J. Keaveney, F. Ponciano-Ojeda, S. Rieche, M. Raine, D. Hampshire, and I. Hughes, Quantitative optical spectroscopy of 87rb vapour in the voigt geometry in dc magnetic fields up to 0.4 t, *Journal of Physics B: Atomic, Molecular and Optical Physics* **52**, 055003 (2019).

[32] F. Ponciano-Ojeda, F. Logue, and I. Hughes, Absorption spectroscopy and stokes polarimetry in a 87rb vapour in the voigt geometry with a 1.5 t external magnetic field, *Journal of Physics B: Atomic, Molecular and Optical Physics* **54**, 015401 (2020).

[33] D. Reed, N. Šibalić, D. Whiting, J. Kondo, C. Adams, and K. Weatherill, Low-drift zeeman shifted atomic frequency reference, *OSA Continuum* **1**, 4 (2018).

[34] D. A. Steck, Rubidium 87 d line data, available online at <http://steck.us/alkalidata> (2025), revision 2.3.4.

[35] C. J. Foot, *Atomic physics*, Vol. 7 (Oxford university press, 2005).

[36] S. Scotto, *Rubidium vapors in high magnetic fields*, Ph.D. thesis, Université Paul Sabatier-Toulouse III (2016).

[37] Center for High Throughput Computing, Center for high throughput computing (2006).

[38] F. S. Ponciano-Ojeda, *Stokes polarimetry and magnetometry using a thermal Rb vapour in the Voigt geometry with large magnetic fields*, Ph.D. thesis, Durham University, Durham, United Kingdom (2021).